ORIGINAL PAPER

Region specific anisotropy and rate dependence of Göttingen minipig brain tissue

Gregory M. Boiczyk[1] · Noah Pearson[2] · Vivek Bhaskar Kote[3,4] · Aravind Sundaramurthy[3,4] · Dhananjay Radhakrishnan Subramaniam[3,4] · Jose E. Rubio[3,4] · Ginu Unnikrishnan[3,4] · Jaques Reifman[3] · Kenneth L. Monson[1,2]

Abstract

Traumatic brain injury is a major cause of morbidity in civilian as well as military populations. Computational simulations of injurious events are an important tool to understanding the biomechanics of brain injury and evaluating injury criteria and safety measures. However, these computational models are highly dependent on the material parameters used to represent the brain tissue. Reported material properties of tissue from the cerebrum and cerebellum remain poorly defined at high rates and with respect to anisotropy. In this work, brain tissue from the cerebrum and cerebellum of male Göttingen minipigs was tested in one of three directions relative to axon fibers in oscillatory simple shear over a large range of strain rates from 0.025 to 250 s^{-1}. Brain tissue showed significant direction dependence in both regions, each with a single preferred loading direction. The tissue also showed strong rate dependence over the full range of rates considered. Transversely isotropic hyper-viscoelastic constitutive models were fit to experimental data using dynamic inverse finite element models to account for wave propagation observed at high strain rates. The fit constitutive models predicted the response in all directions well at rates below 100 s^{-1}, after which they adequately predicted the initial two loading cycles, with the exception of the 250 s^{-1} rate, where models performed poorly. These constitutive models can be readily implemented in finite element packages and are suitable for simulation of both conventional and blast injury in porcine, especially Göttingen minipig, models.

Keywords Biomechanics · Inverse finite element modeling · Brain · Viscoelasticity · Anisotropy · Oscillatory shear

1 Introduction

Traumatic brain injury (TBI) is a significant cause of injury and death in both civilian and military populations. In the United States (U.S.) alone, TBI accounts for approximately 2 million emergency department visits and over 69,000 deaths per year (Centers for Disease Control and Prevention 2023). In addition, nearly 480,000 U.S. Service members sustained at least a mild TBI between 2000 and 2023 (Military Health System 2023). In order to develop mitigation strategies for traumatic brain injury, the underlying biomechanics and mechanisms of TBI need to be better understood. Finite element (FE) simulations are a vital tool for understanding the biomechanics of head injury (Dixit and Liu 2016; Madhukar and Ostoja-Starzewski 2019; Sundaramurthy et al. 2012; Sundaramurthy et al. 2021). The results of these models are highly dependent on the material parameters used (Zhao et al. 2018). For simulations to be accurate, material parameters should be based on the modeled loading rates and modes. High-quality constitutive models are especially needed for the brain where despite decades of experimental modeling, reported properties still show a wide range of variation (Meaney et al. 2014).

✉ Gregory M. Boiczyk
gregboiczyk@gmail.com

1 Department of Biomedical Engineering, University of Utah, Salt Lake City, UT, USA

2 Department of Mechanical Engineering, University of Utah, Salt Lake City, UT, USA

3 Telemedicine and Advanced Technology Research Center, Department of Defense Biotechnology High Performance Computing Software Applications Institute, United States Army Medical Research and Development Command, Fort Detrick, MD, USA

4 The Henry M. Jackson Foundation for the Advancement of Military Medicine, Inc., Bethesda, MD, USA

Peak strain rates seen in FE models of TBI can vary by several orders of magnitude depending on the type of injury being simulated (e.g., blast vs. impact), species, and material models used in the simulation. For example, in simulations of human blast injury, strain rates have been observed on the order of ten (Subramaniam et al. 2021; Zhang et al. 2013) to several hundred per second (Singh et al. 2014). In contrast, peak strain rates in simulations of impact injury have been observed at up to 235 s^{-1} in porcine models compared to 65 s^{-1} in humans (Wu et al. 2021). Consequently, constitutive models should be generated from experimental data over a broad range of strain rates.

Oscillatory shear testing, either with a parallel plate shear tester or a rheometer, is a long-established means of testing brain tissue. Most of these studies have been limited to either strain rates below 50 s^{-1} (Bilston et al. 1997, 2001; Brands et al. 2000; Budday et al. 2017b; Chatelin et al. 2012; Feng et al. 2013; Hrapko et al. 2008) or low strain amplitudes (below 5% shear strain) (Bilston et al. 1997, 2001; Brands et al. 2000; Chatelin et al. 2012; Feng et al. 2013; Hrapko et al. 2008; Nicolle et al. 2004), with few studies examining both high strain rates and large deformations. Darvish and Crandall (Darvish and Crandall 2001) subjected bovine cerebral tissue to oscillations at frequencies of 1–1000 Hz at amplitudes of up to 10.5% shear strain but, due to the effects of resonance in their experimental system, were not able to use any rates above 30 Hz to develop constitutive models. Arbogast and Margulies (Arbogast and Margulies 1998) subjected porcine brainstem samples to frequency sweeps between 20 and 200 Hz at amplitudes of up to 7.5%; while, Thibault and Margulies (Thibault and Margulies 1998) subjected porcine cerebral tissue to frequency sweeps between 20 and 200 Hz at amplitudes up to 5%. However, both studies modeled the tissue response using linear viscoelasticity and did not attempt to fit data to a hyper-viscoelastic framework. To date, no author has performed oscillatory shear experiments at both high strains (over 10%) and high strain rates (up to 200 s^{-1}) and developed a respective hyper-viscoelastic model.

Brain tissue anisotropy at strain rates and strains remains poorly characterized. Brain tissue is broadly classified as either white or gray matter. Gray matter primarily comprises neuronal cell bodies and glial cells; while, white matter contains axons that connect neurons and glial support cells. Most of these axons, especially those of larger diameter (Simons and Trajkovic 2006), are wrapped in myelin sheaths. In addition to their critical physiological functions, myelin content is correlated with increased tissue stiffness (Weickenmeier et al. 2017), suggesting that they may act as reinforcing fibers within the brain. In many regions of the brain, such as corpus callosum (Budde and Annese 2013) and corona radiata (Budday et al. 2017a), these fibers run in a predominant direction and may lead

to a significant degree of anisotropy. In these regions, axon fiber direction can be mapped throughout the brain using diffusion tensor imaging (DTI) (Budde and Annese 2013; Budday et al. 2017a). Many studies have examined anisotropy in the brain. For example, Arbogast and Margulies demonstrated that the brainstem is transversely isotropic in shear with a single preferred fiber direction (Arbogast and Margulies 1998). In a transversely isotropic material, the shear response is stiffer in the preferred direction where the fibers run in the shear plane and normal to the direction of shear, as compared to the non-preferred orientations where the fibers run either transverse to the shear plane or in the shear plane but aligned with the direction of shear, which will respond similarly. In the cerebrum, published data on anisotropy are mixed, with some studies reporting that the region demonstrates significant anisotropy (Darvish and Crandall 2001; Feng et al. 2013; Velardi et al. 2006), with others reporting an isotropic response (Budday et al. 2017a; Nicolle et al. 2005). To date, no studies have examined the effects of anisotropy in cerebellar tissue.

Previous work by our group focused on characterizing brain tissue from adolescent (aged 4–5 months) Göttingen minipigs, when brain tissue properties are similar to those of adult pigs (Prange and Margulies 2002), in high-rate and quasi-static (QS) shear and compression (Boiczyk et al. 2023). While we produced hyper-viscoelastic constitutive models that predict the response of brain tissue in shear and compression at strain rates up to 300 s^{-1}, our experimental data did not include intermediate strain rates in the several decades between the quasi-static and high-rate tests. This work also suggested that our simple shear experiments may have been confounded by inhomogeneous deformations in part due to wave propagation at high rates, potentially stiffening the response. If this is the case, conventional methods of fitting constitutive models may provide poor fit quality and not accurately reflect the experimental results. While such issues may be unavoidable in high-rate brain tissue testing, inverse FE modeling can be used to account for dynamic effects. Recently, multiple studies have investigated the use of inverse methods to successfully fit hyperelastic (Feng et al. 2017; Kaster et al. 2011; MacManus et al. 2017; Moran et al. 2014), as well as hyper-viscoelastic (Felfelian et al. 2019; Hosseini-Farid et al. 2019) and biphasic (Hosseini-Farid et al. 2020), constitutive models to experimental tests of brain tissue. However, none of these studies has used these methods to model simple shear in brain tissue at high rates. The literature either focuses on compressive loading or only considers simple shear using rate-independent hyperelastic models.

In this study, we performed a new set of experiments where tissue from the cerebrum and cerebellum of adolescent male Göttingen minipigs was subjected to simple shear

frequency sweeps at rates between 0.025 and 250 s^{-1} over large sub-failure deformations. Tissue from each region was tested in three different directions and was used to define a transversely isotropic hyper-viscoelastic constitutive model for each region using inverse FE methods.

2 Methods

2.1 Overview

Brain tissue samples from the cerebrum and cerebellum were obtained from freshly euthanized Göttingen minipigs and tested in one of three directions relative to tractography-determined axonal fiber directions. Average experimental data were used to fit both isotropic and transversely isotropic hyper-viscoelastic constitutive models using both analytical and inverse FE methods.

2.2 Sample preparation

The Animal Care and Use Review Office of the US Army Medical Research and Development Command, Fort Detrick, MD, and the Institutional Animal Care and Use Committee at the University of Utah approved all experimental protocols. Tissue was harvested from 20 juvenile male Göttingen minipigs (4–5 months old). Pigs were euthanized immediately before tissue harvest via an overdose of phenytoin/pentobarbital. The braincase was carefully opened with a hammer and chisel, and the brain was freed from the dura and cranial nerves before being removed intact and immersed in a solution of 7.5% polyethylene glycol buffered (PEG) saline (7.5% by weight polyethylene glycol in phosphate-buffered saline) (Lujan et al. 2009) until testing. To prevent potential material property changes due to differing temperatures between samples from confounding our results, all tissue was stored and tested at room temperature (21 °C).

Diffusion tensor imaging was obtained from one animal to define brain tractography. The excised brain was imaged at the Preclinical Imaging Core Facility (University of Utah) with a 7 T MRI (Bruker BioSpec, Ettlingen, Germany). Resulting diffusion tensor imaging (DTI) and T2 MRI data were evaluated in DSI Studio (Yeh et al. 2013) to determine fiber directions and identify suitable sites for tissue harvest in the cerebrum and the cerebellum. In the cerebrum, a region of the corona radiata with fibers running predominantly rostral caudally was chosen (Supplemental Fig. 1), while in the cerebellum a region with fibers running predominantly medial laterally was chosen (Supplemental Fig. 2). All tissue samples used for mechanical characterization were harvested from these
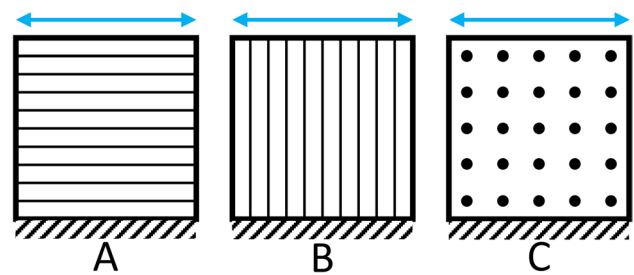

Fig. 1 Schematic of the *A*, *B*, and *C* directions relative to axon fiber direction (black lines and dots) and direction of applied shear (blue arrows)

regions in one of three directions based on predominant fiber orientation (Fig. 1). Tissue was tested in either the A direction (non-preferred), where the fibers run in the shear plane and parallel to the direction of shear; the B direction (preferred), where the fibers run in the shear plane and normal to the direction of shear; or the C direction (non-preferred), where fibers run normal to both the shear plane and the direction of shear (Arbogast and Margulies 1998).

Immediately before testing, tissue was cut, using a custom die, to a cuboid with a size of 8 mm wide by 8 mm long and 5 mm thick in one of the three fiber orientations. A scalpel was run over the top face of the die to ensure a uniform thickness of the specimen and remove any excess brain tissue. A total of 2–4 samples were harvested from the cerebrum and cerebellum of each animal for a target sample size of 12 per group (region and direction). After cutting, tissue samples were measured with digital calipers, and dimensions were recorded. Tissue samples were then immediately mounted between parallel aluminum plates on a custom oscillatory shear tester with a thin layer of cyanoacrylate adhesive. Due to the high driven strain rates used in these tests, tissue could not be tested in a bath. Tissue samples were instead inspected between each applied frequency, and additional PEG-buffered saline was applied as needed to keep the tissue hydrated.

2.3 Tissue tester

All material characterization was performed on a custom oscillatory shear testing device developed for this study (Fig. 2). The top plate was connected to a 250 g load cell (Model 31 Low, Honeywell, Golden Valley, MN); while, the bottom plate was connected to a voice coil actuator (LAS16-23, BEI Kimco, Vista, CA) controlled via a servo amplifier and driver (412CE, Copley Controls, Canton, MA). Load and displacement data were acquired from the load cell and an integrated Hall effect sensor in the voice coil, respectively, via a data acquisition unit (SCXI-1520, National Instruments, Austin, TX) using a custom LABVIEW VI.
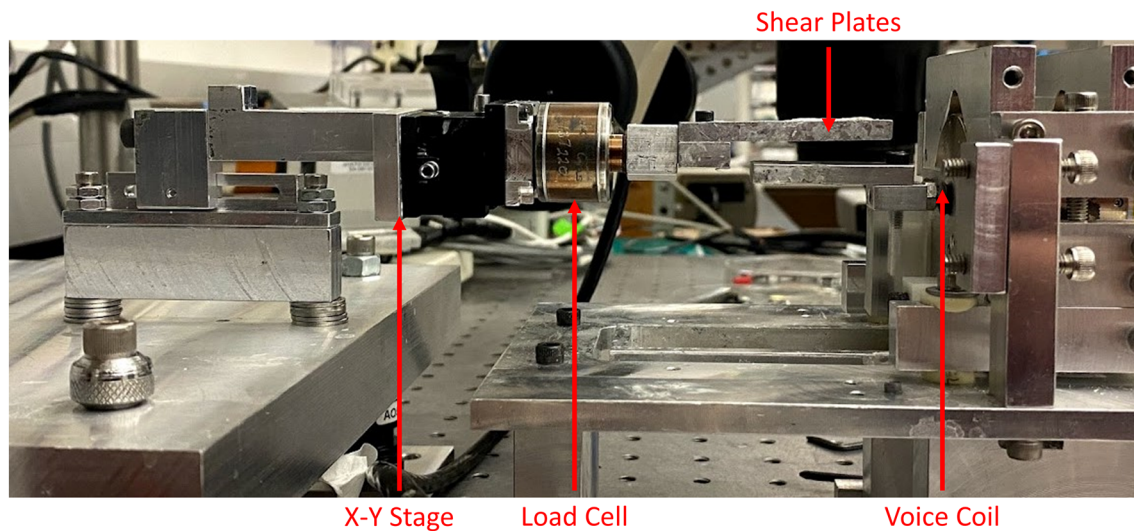
Fig. 2 Custom shear tester

2.4 Oscillation tests

Each sample was subjected to a frequency sweep composed of five shear strain oscillations with an amplitude of 20% at rates of 0.025. 0.25, 2.5, 12.5, 50, 100, 125, and 250 s^{-1} (corresponding to driven frequencies of 0.02, 0.2, 2, 10, 40, 80, 100, and 200 Hz) around a mean shear strain of 0%. Data were simultaneously sampled from the load cell and displacement sensor with a sample rate of 100 times the driven frequency (between 2 and 20 kHz) such that there were 500 data points for every oscillation.

A total of 72 samples were subjected to testing, comprising 36 samples harvested from the cerebrum and an additional 36 from the cerebellum. Within these 36 samples, 12 were tested in each of the *A*, *B*, and *C* directions. All samples underwent five cycles of oscillatory loading at eight different strain rates, ranging from 0.025 to 250 s^{-1}.

2.5 Data processing

Load- and displacement–time series data were filtered using a phaseless four-pole Butterworth filter specified in the SAE J211 standard (Bell et al. 2018) with a cutoff frequency of ten times the driven frequency (Supplemental Figs. 3 and 4). The 1st Piola–Kirchhoff (1st PK) shear stress (*T*) was then calculated by dividing the load signal by the cross sectional sample area (the product of tissue length and width). Shear strain (*K*) was defined as the ratio of displacement to specimen height.

While brain tissue mechanical response is nonlinear, dynamic modulus was calculated as a reference for simple comparisons between different strain rates, regions and loading directions. The value was calculated at each driven strain rate by first identifying the locations of the peaks and troughs in the oscillatory stress and strain data using the findpeaks function in MATLAB. The locations of these peaks and troughs were then used to calculate the amplitudes of the first cycles of the stress and strain waveforms, T_0 and K_0, respectively. These amplitudes were used to calculate the dynamic modulus using Eq. 1. Finally, the phase angle (ϕ) was calculated using the cross-correlation function *xcorr* in MATLAB.

$$G = \frac{T_0}{K_0} \tag{1}$$

For each region and direction, we calculated the average shear stress and shear strain waveforms by first re-sampling the stress and strain data from each individual sample such that each sample had values at the same discrete time points. We then computed the average and standard deviation of the re-sampled stress and strain waveforms which were used for all subsequent analysis.

2.6 Statistical analysis

To determine whether region-specific or anisotropic constitutive models were needed, the effects of tissue anisotropy and tissue region were examined by comparing the dynamic moduli across all strain rates. First, a multivariate ANOVA was performed to compare the effects of oscillatory strain rate, region, and direction on dynamic modulus. Where a statistical difference ($p < 0.05$) was detected, a Tukey Test was performed to evaluate pairwise differences

in either region, tissue direction, or the combination of region and direction. To correct for multiple comparisons, we defined significance for the Tukey test results as values below a Bonferroni corrected value of $p = 0.016$.

2.7 Constitutive modeling

To evaluate the effects of modeling with and without assuming deformation homogeneity, constitutive models were fit using MATLAB and inverse FE methods, respectively. Methods and results associated with the MATLAB fits are detailed in the Appendix.

FE models were constructed in FEBio (Maas et al. 2012) for each of the three directions in the cerebrum and cerebellum (6 FE models total). As we were primarily interested in wave propagation along the direction of loading as well as through the thickness of the sample, all models consisted of a half-symmetry, 8 mm long, 4 mm wide (half the width of the experimental specimen), and 5 mm tall cuboid of brain tissue (Supplemental Fig. 5), with symmetry boundary conditions (constrained Y) applied to the positive Y face. The top face of the brain model was connected to a fixed, 1 mm thick rigid plate via a rigid contact to mimic the experimental conditions of the brain tissue connected to the load-cell-side plate in our shear tester. We did not explicitly model the bottom, moving plate in this simulation. Instead, we constrained the displacement in the Y- and Z-directions of the bottom face of the brain tissue and applied a sinusoidal displacement in the X-direction defined by the experimental average strain vs. time data for each region.

Brain tissue was modeled as a nearly incompressible viscoelastic material with a solid (matrix–fiber) hyperelastic mixture. We used an Ogden model to represent the matrix component of the solid mixture. In order to capture anisotropy, we opted to also use a fiber with exponential-power law material in FEBio (Maas and Weiss 2007) with the deviatoric fiber stress given by Eq. 2,

$$\tilde{\sigma} = H\left(\widetilde{I}_n - 1\right)\frac{2\widetilde{I}_n}{J}\frac{\partial \tilde{\psi}}{\partial \widetilde{I}_n}\boldsymbol{n} \otimes \boldsymbol{n} \tag{2}$$

where $H(x)$ is the Heaviside step function that ensures fibers only contribute in tension, $\widetilde{I}_n$ is the invariant defined by the square of the deviatoric fiber stretch $\tilde{\lambda}$ (Eq. 3),

$$\widetilde{I}_n = \tilde{\lambda}^2 = \boldsymbol{n}_r \cdot \widetilde{C} \cdot \boldsymbol{n}_r \tag{3}$$

where $\widetilde{C}$ is the deviatoric right Cauchy–Green tensor, and the unit vector along the fiber in the reference configuration $\boldsymbol{n_r}$ is related to the unit vector along the fiber in the current configuration $\boldsymbol{n}$ (Eq. 4).

$$\boldsymbol{n} = \tilde{F} \cdot \boldsymbol{n}_r / \tilde{\lambda} \tag{4}$$

The strain energy function for this fiber is given by Eq. 5,

$$\tilde{\psi} = \frac{\xi}{\alpha\beta}\left(\exp\left[\alpha\left(\widetilde{I}_n - 1\right)^{\beta}\right] - 1\right) \tag{5}$$

where $\xi > 0$ is the fiber modulus, $\alpha \geq 0$ is the coefficient of the exponential argument, and $\beta \geq 2$ is the power of the exponential argument.

A convergence study was performed to examine the optimal element type and number of elements by comparing the magnitude and timing of the first X-reaction peak force in the model. The model was considered converged when there was less than a 1% change in the magnitude of the first peak X-reaction force and the time at which it occurred. We evaluated meshes with grid sizes ranging from 5 to 40 elements in the Z direction and 2–40 elements in the Y direction for both 8- and 20-node hexahedral elements. The optimal models were meshed with 400 HEX8 (8-node hexahedral) elements, with eight elements in the X direction, two in the Y direction, and 25 in the Z direction.

Optimization of all matrix and viscoelastic parameters was performed in the non-preferred (A) direction for each region, preserving the other non-preferred (C) direction for validation testing. Optimal material parameters for the constitutive models were found using the built-in FEBio optimization functionality. To reduce computational time, we leveraged the convolution integral present in the formulation of the hyper-viscoelastic constitutive model to optimize parameters at the strain rates closest to the corresponding time constant and all rates preceding that rate. To this end, the hyperelastic parameters (c, m) were optimized for the quasi-static (QS) oscillations of 0.025 s^{-1}, g_1 was optimized for all oscillations through 0.25 s^{-1}, g_2 was optimized for all oscillations through 12.5 s^{-1}, g_3 was optimized for all oscillations through 125 s^{-1}, and $g_4 - g_5$ were optimized for all oscillations up through 250 s^{-1}. Optimization of the three fiber-specific parameters (ξ, α, β) was performed on all oscillations at 0.025 s^{-1} for each region's preferred (B) direction, preserving all subsequent rates for validation. In order to reduce the likelihood that the optimized solution was settling on a local minimum, multiple parameter scans where given parameters were varied by a defined step size between upper and lower bounds were run. Initially, a large range of values was scanned with a large step size. Subsequent scans were then performed with a progressively narrowing range and decreasing step size until a scan with a step size of 10 (c, ξ) or 1 (m, α, β, g_i) was performed. An optimization was then run with the initial condition for a given parameter defined as the value with the lowest objective value from the final parameter scan.

3 Results

3.1 Experimental observations

Due to early issues in data acquisition triggering and testing errors resulting from poorly adhered or deficient samples, the total sample size in all groups differed slightly from the 12 samples targeted. In the cerebrum, the sample size for each direction was $A = 12$, $B = 10$, and $C = 11$, while in the cerebellum, the sample size for each direction was $A = 10$, $B = 12$, and $C = 12$.

Average stress–strain (hysteresis) curves for the cerebrum in the A, B, and C directions are shown in Figs. 3, 4, 5, respectively; while, hysteresis curves for the cerebellum in the A, B, and C directions are shown in Supplemental Figs. 6–8, respectively. For all strain rates below 250 s^{-1}, the resulting stress–strain curve for these tests begins in the lower-left quadrant and advances toward the lower right quadrant in a clockwise direction. At 250 s^{-1}, the stress–strain curves advance from the lower left quadrant to the upper left quadrant in a counterclockwise direction. The curves show substantial degrees of hysteresis for all rates, regions, and directions tested, with the brain being significantly stiffer during loading than unloading. Comparisons between the first and last (fifth) loading cycles of each strain rate show that the first cycle was stiffer than the last for all but the highest rates. For all regions and directions, the first applied oscillation of 0.025 s^{-1} shows the most dramatic

change between the first and last cycle, likely due to preconditioning of the sample.

In tests with strain rates below 100 s^{-1}, prescribed displacement waveforms showed minimal variation from the target amplitude of $K = 0.2$ for five cycles at a given driven frequency. At rates of 100–250 s^{-1}, drift was present in the displacement waveform, with subsequent loading cycles applying higher amplitudes. However, this was consistent between tests, and peak deformation stayed below $K = 0.25$.

Measured stress–strain waveforms showed greater variability, especially at high rates. Additionally, some degree of load cell drift is present in the raw load signal at the lowest rate of 0.025 s^{-1}, which is not evident at higher rates and contributes to the apparent increase in the magnitude of stresses due to negative deformations seen at this rate. For oscillations at and above 50 s^{-1}, the amount of noise in the stress data increases significantly. This is particularly evident in the 100 and 125 s^{-1} rates, where the hysteresis curves appear to cross over each other at several points, most noticeably in Figs. 3 and 5. The change in curve directionality observed at 250 s^{-1} appears to be due to a change in the phase of stress and strain, with the stress curve beginning to lag the strain curve rather than preceding it as at other rates. Generally, the preferred and non-preferred directions showed similar noise levels with the exception of the 50 s^{-1} where a significant spike in noise is present in the stress data for the preferred directions but is absent in the non-preferred directions.

Fig. 3 Shear stress (average ± standard deviation)–shear strain hysteresis curves for the cerebrum in the non-preferred (*A*) direction (*N* = 12)
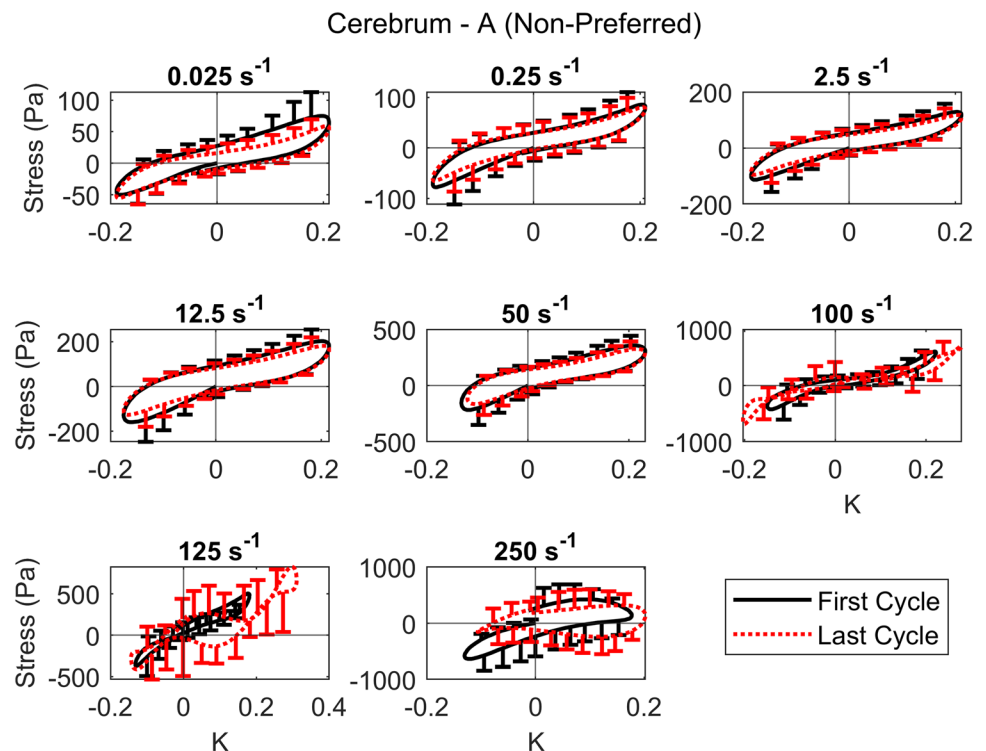
Fig. 4 Shear stress (average ± standard deviation)–shear strain hysteresis curves for the cerebrum in the preferred (*B*) direction (*N* = 10)
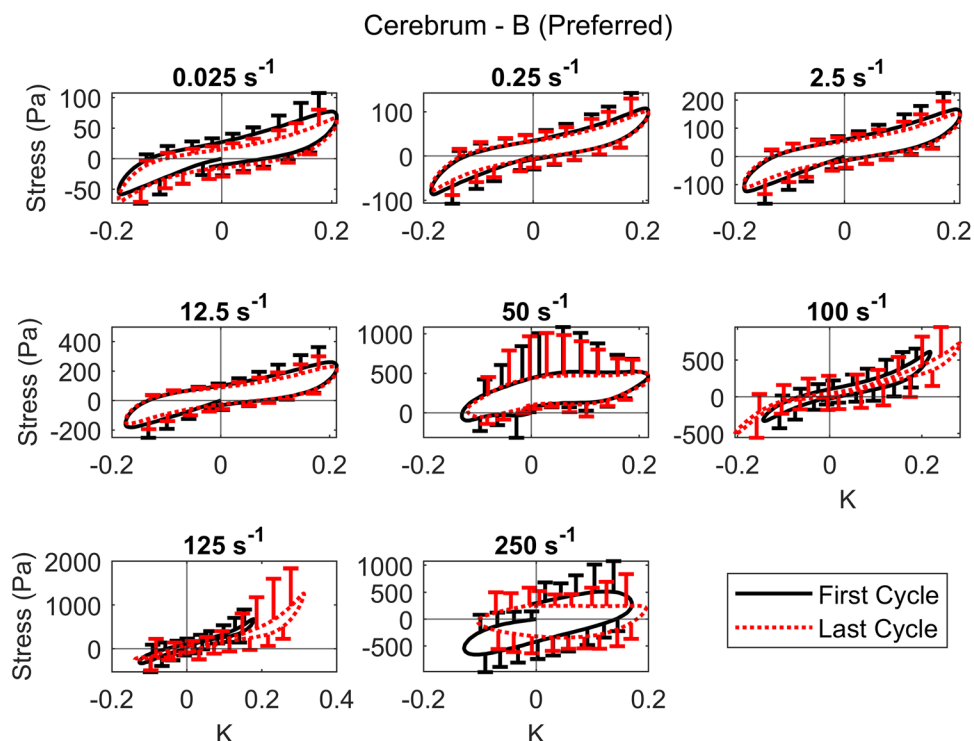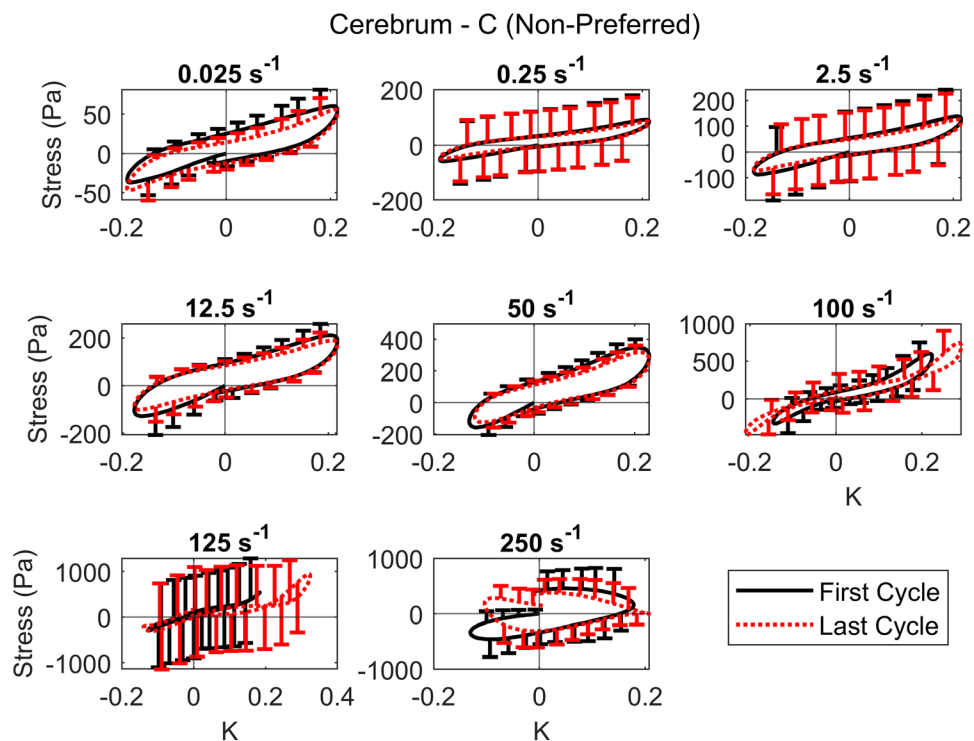

Fig. 5 Shear stress (average ± standard deviation)–shear strain hysteresis curves for the cerebrum in the non-preferred (*C*) direction (*N* = 11)

For all directions and regions, dynamic modulus increased nonlinearly from rates of 0.025–50 s^{-1} before decreasing slightly at 100 s^{-1}, with the means of some groups continuing to decrease; while, others leveled out or began to increase again (Fig. 6). There is also a noticeable increase in scatter at the highest rates, potentially a result of increased experimental noise from both high frequency electrical sources and increased mechanical vibrations. Multivariate ANOVA suggested significant differences ($p < 0.01$) between loading directions for both

Fig. 6 Dynamic modulus (average ± standard deviation) as a function of strain rate and loading direction for the cerebrum and cerebellum
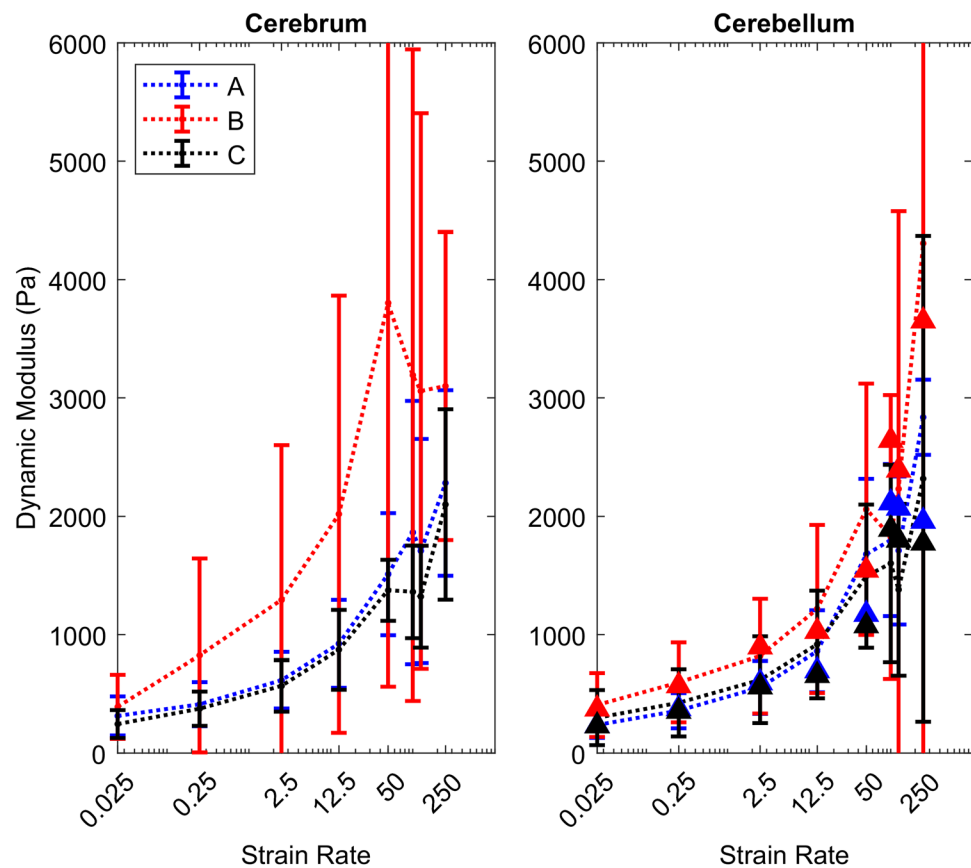
the cerebrum and cerebellum. In the cerebrum, pairwise t tests showed that the *B* direction was significantly stiffer than both the A ($p < 0.001$) and C ($p < 0.001$) directions, which did not significantly differ ($p = 0.58$). Pairwise *t*-tests in the cerebellum showed that the B direction was significantly stiffer than the *C* direction ($p = 0.008$) but not the A direction ($p = 0.08$). As in the cerebrum, the *A* and *C* directions in the cerebellum showed no significant difference ($p = 0.76$). While no significant difference was present between the A and B directions, the mean dynamic modulus is noticeably higher at all rates in the B direction compared to the A direction, which has comparable means to the *C* direction. Thus, our results suggest that brain tissue from both the cerebrum and cerebellum shows a transversely-isotropic response, with the preferred direction being the B direction.

For all regions and directions, the stress waveform led the strain waveform by approximately 20 degrees between 0.025 and 12.5 s^{-1} before increasing to around 40 degrees at a rate of 50 s^{-1} (Fig. 7). At 100 s^{-1}, there was considerable variation in phase angle, with stress leading strain between 50 and 60 degrees in the cerebrum and 36 and 63 degrees in the cerebellum. Some individual samples showed a phase lag at this rate, where the stress

waveform began to lag the strain waveform, leading to more variation in the data. At 125 s^{-1}, the mean phase angle decreased and a similarly large degree of variance to the 100 s^{-1} rate was present, with some, but not all, samples exhibiting phase lag. At 250 s^{-1}, the mean phase angle for all groups ranged between -6 and -65 degrees, and almost all individual samples show some degree of phase lag.

3.2 Constitutive modeling

FEBio simulations for low-rate cases resulted in model fits similar to those assuming a homogeneous deformation, but substantial differences were apparent at higher rates. At the lower rates (0.025 and 12.5 s^{-1}), shear stress distributions were closely similar to one another, all showing the broadly uniform stress distribution in the center shear plane observed for 0.025 s^{-1} (Fig. 8). However, areas of lower stress develop on the left and right sides of the model, and regions of higher stress are seen in the four corners of the model at the rigid plate and fixed boundaries. Generally, the model remains cuboidal even at high deformations at the lower rates, though some curvature develops in the elements at the rigid contact and fixed boundaries. At 50 s^{-1}, the model exhibits a similar

Fig. 7 Phase angle (average ± standard deviation) phase angle as a function of strain rate and loading direction for both the cerebrum and cerebellum
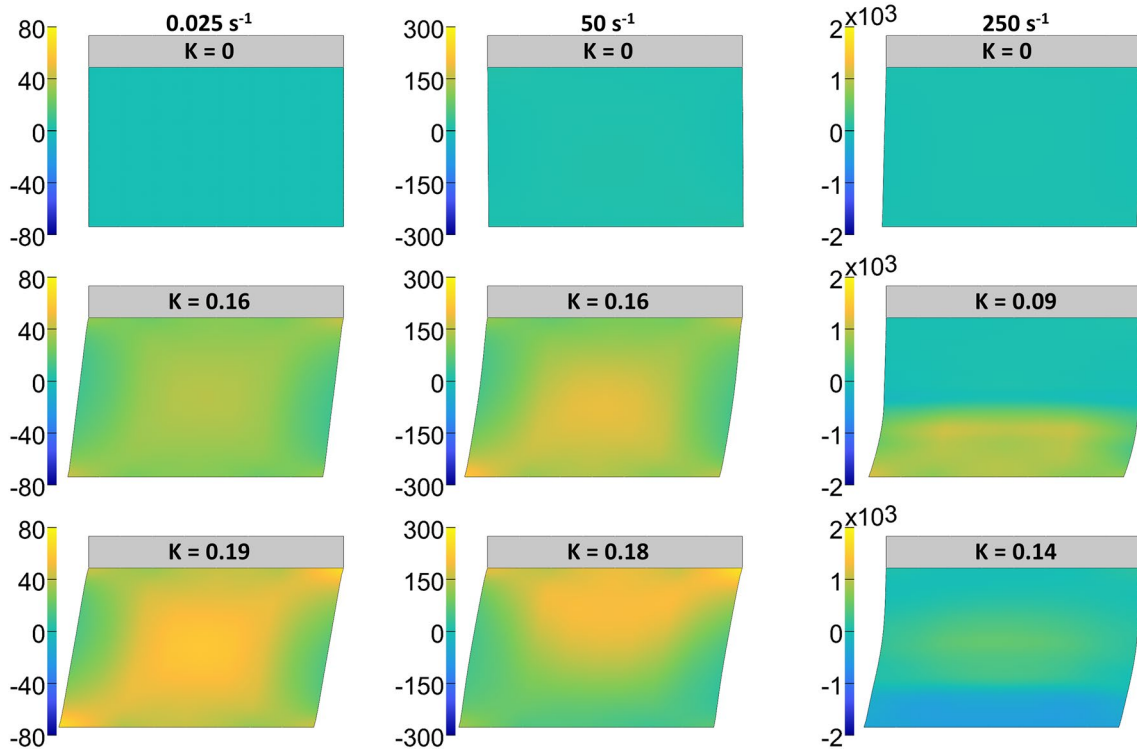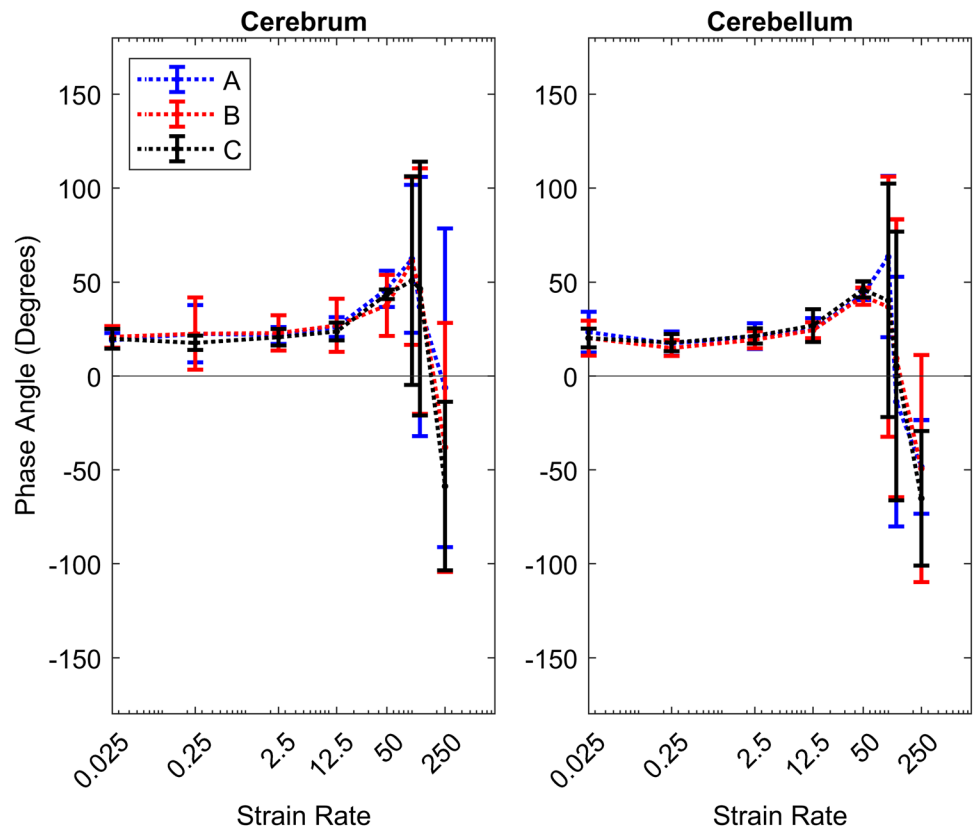

Fig. 8 Shear (*XZ*) stress distribution at the center plane for the cerebral finite element model during the first loading cycle at 0.025, 50, and 250 s.$^{-1}$

stress distribution to lower rates at low strains ($K < 0.1$) but develops a noticeable stress concentration in the top half of the model as strains increase. At higher strains, the model develops a slight curvature on the left and right sides, with the side facing the direction of motion becoming slightly concave. When the motion stops at the peak or minimum of the sinusoidal oscillation, the model recovers a roughly cuboidal state similar to lower rates. At the three highest rates (100–250 s^{-1}), substantial wave propagation is present in the model, with stress waves noticeably developing at the bottom, oscillating face, and advancing toward the rigid contact at the top face. The model also develops substantial curvature at these rates as the stress wave propagates through the sample. These effects become especially pronounced at 250 s^{-1}.

Visual inspection of the models shows the tendency of the inverse FE model to somewhat overpredict the magnitude of maximum and minimum stresses to varying

Fig. 9 Experimental data and inverse finite element fits for the cerebrum in the *A* (non-preferred) direction
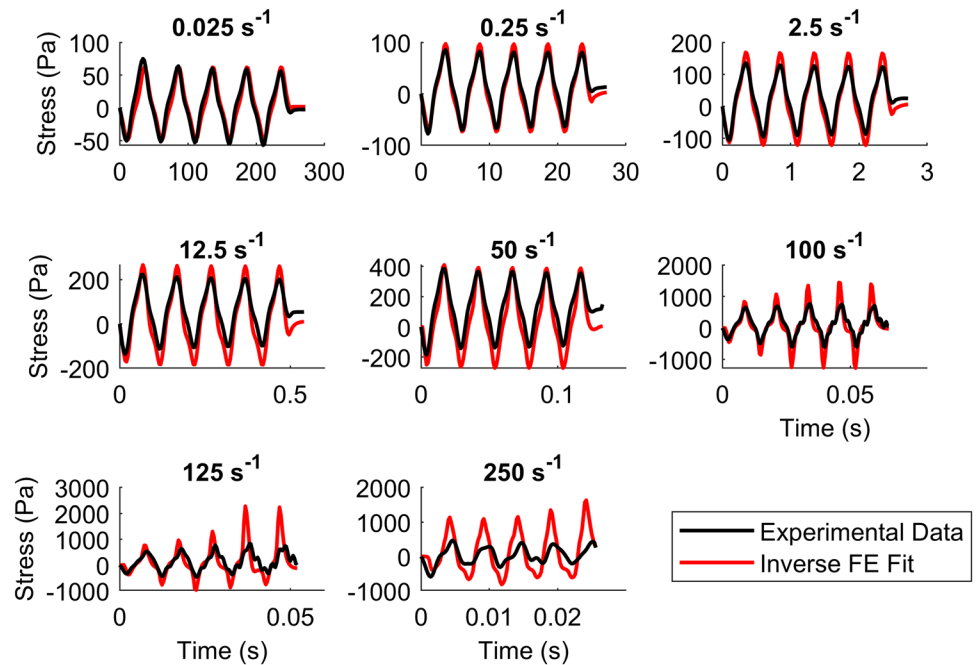

Fig. 10 Experimental data and inverse finite element fits for the cerebrum in the *B* (preferred) direction
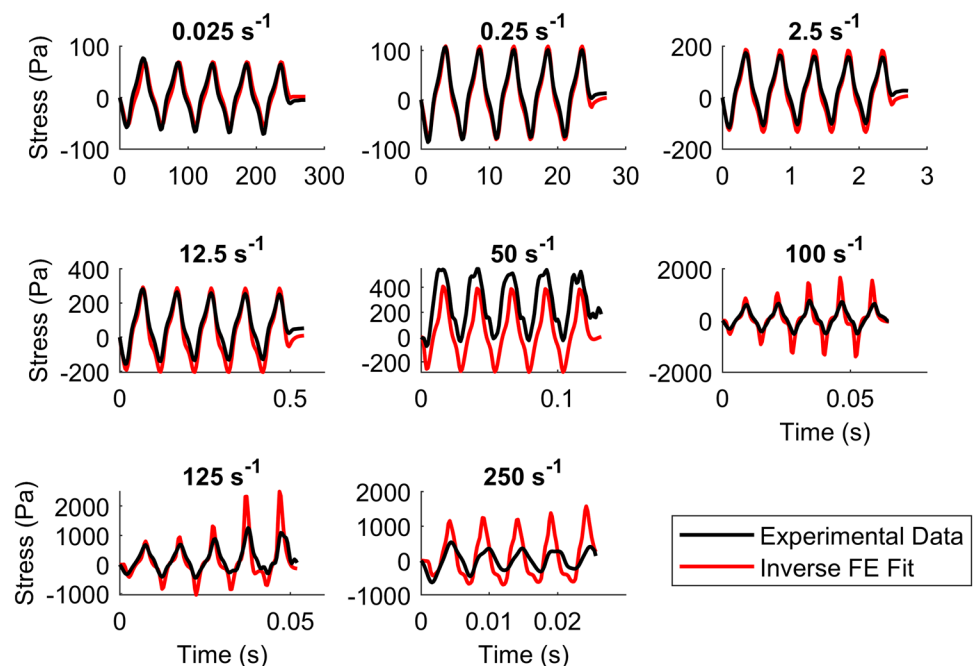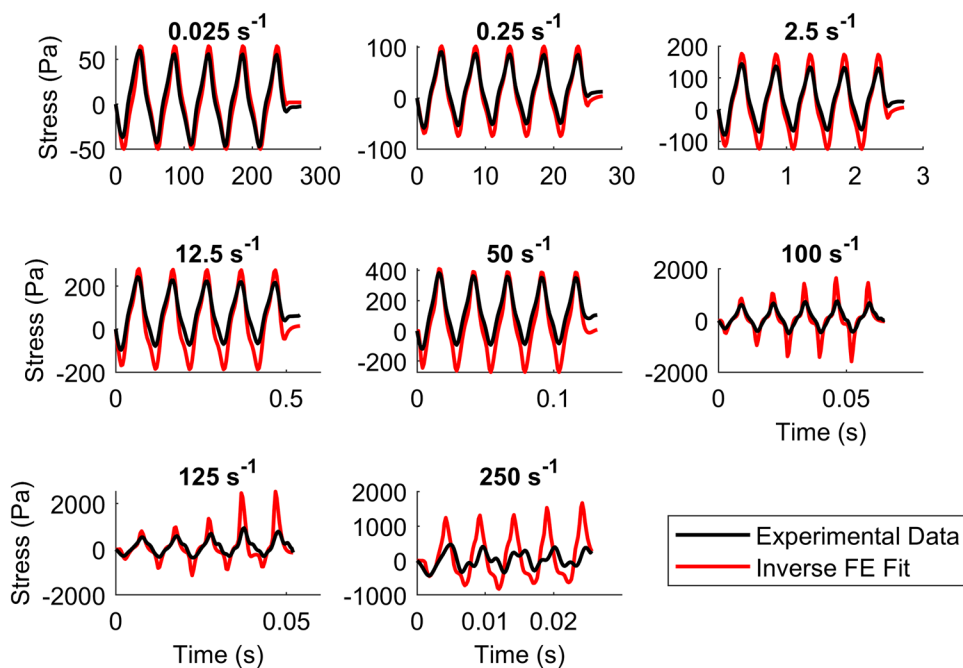
Fig. 11 Experimental data and inverse finite element fits for the cerebrum in the *C* (non-preferred) direction

degrees in all directions and at all rates, with the biggest degree of overprediction seen in the *C* direction. At 125 s^{-1}, the model tends to overpredict the magnitude of stresses after the first two oscillations and overpredicts the magnitude after the first trough at 250 s^{-1}. FE-derived (X-reaction force) stress predictions in the cerebrum for all oscillations are compared to experimental stresses in the *A*, *B*, and *C* directions in Figs. 9, 10, 11, respectively.

To examine model fit quality, we calculated the overall root mean squared error (RMSE) between regularized experimental and model stress data as well as the phase angle between these waveforms. Note that the phase angle and RMSE are not independent of one another, with both phase and amplitude error contributing to overall error. Error and phase angle values for the cerebrum at all rates for each of these directions are shown in Table 1. For all directions, the lowest rate of 0.025 s^{-1} shows a relatively high degree of phase shift and error (due to both phase mismatch and overprediction of stress magnitude,

particularly in the C direction). Error and the magnitude of phase shift are substantially lower between 0.25 and 50 s^{-1}, with the highest error in the A direction. Above 50 s^{-1}, both overall error and phase shift increase, with all directions showing some negative phase shift, indicating the model is leading the experimental data somewhat at these rates. At 100 and 125 s^{-1}, the MATLAB fits have a similar or lower phase angle to the inverse FE fits, while at 250 s^{-1}, the inverse FE fits have a lower phase shift.

Inverse FE fits for the cerebellum are shown in Supplemental Figs. 9–11 for the *A*, *B*, and *C* directions, respectively. Table 2 shows the phase angle difference and overall RMSE error for the cerebellar fits. Similar to the cerebrum, error, and phase angle are relatively high for all regions at 0.025 s^{-1}, due to both a high degree of phase shift as well as overprediction of stress magnitude, before decreasing for rates up to 100 s^{-1}. However, error and phase are notably higher at these rates, with a pronounced increase above 12.5 s^{-1}. At 100 s^{-1}, there is a lower degree of phase shift

Table 1 Overall error (RMSE) and phase angle between regularized model and experimental stresses for the cerebrum inverse finite element fits for all directions

Direction	Error mode	Strain rate (s⁻¹)							
		0.025	0.25	2.5	12.5	50	100	125	250
A	Phase (°)	13.68	0.7	0.7	0.7	4.3	− 9.4	− 24.5	− 30.2
	RMSE	0.31	0.2	0.2	0.2	0.2	0.4	0.7	0.8
B	Phase (°)	13.7	1.4	1.4	1.4	16.6	− 12.2	− 13.0	− 31.7
	RMSE	0.3	0.1	0.1	0.1	0.4	0.5	0.5	0.8
C	Phase (°)	15.1	2.2	1.4	1.4	5.0	− 9.4	− 15.1	− 48.3
	RMSE	0.3	0.1	0.1	0.2	0.2	0.4	0.6	1.0

Negative phase shift denotes model leads experimental data

compared to the cerebrum though error values remain high. Visual inspection of the plots shows that the cerebellar models tend to underpredict maximum while slightly overpredicting minimum stress, especially at rates below 100 s^{-1} and in the C direction. Fits for the 100 s^{-1} and 125 s^{-1} rates are better than in the cerebrum though they degrade in quality after the second oscillation. In contrast to the cerebrum, the model poorly fits the initial loading at 250 s^{-1} before better-predicting stresses at subsequent oscillations, which is especially notable in the A and C directions. Table 3 shows the optimized parameters for both the cerebrum and cerebellum models. The models have similar Ogden model components, though the cerebellum model has a higher shear modulus and lower non-linearity parameter than the cerebrum model. The viscoelastic components are similar at lower rates for both models, but the cerebrum model has higher values at g_3 and g_5, suggesting increased sensitivity to high-rate loading. The cerebrum model also exhibits a much lower degree of anisotropy than the cerebellum model, with a fiber stiffness (ξ) and an exponential coefficient (α) over five times higher in the cerebellum model compared to the cerebrum model.

Table 2 Overall error (RMSE) and phase angle between regularized model and experimental stresses for the cerebellum inverse finite element fits for all directions

Direction	Error mode	Strain rate (s^{-1})							
		0.025	0.25	2.5	12.5	50	100	125	250
A	Phase (°)	13.7	1.4	8.6	15.1	7.9	− 2.9	− 13.0	− 15.1
	RMSE	0.3	0.1	0.2	0.3	0.2	0.4	0.5	0.8
B	Phase (°)	13.7	2.2	8.6	15.1	6.5	− 2.2	− 3.6	30.2
	RMSE	0.3	0.1	0.2	0.3	0.2	0.5	0.6	0.9
C	Phase (°)	15.1	2.9	9.3	18.0	10.8	− 1.4	− 7.9	10.8
	RMSE	0.3	0.1	0.2	0.4	0.3	0.4	0.5	0.6

Negative phase shift denotes model leads experimental data

Table 3 Optimized parameters from the inverse finite element models of the cerebrum and cerebellum

Region	Parameter									
	c (Pa)	m	g_1	g_2	g_3	g_4	g_5	ξ (Pa)	α	β
Cerebrum	323.0	22.1	0.8	1.1	3.1	0.0	92.2	300.0	4.6	2.0
Cerebellum	352.4	16.3	0.9	1.1	0.0	0.0	65.1	1611.0	24.6	2.0

Fig. 12 Predicted stresses from the constitutive model in single ramp, homogeneous simple shear (XZ) for the cerebrum and cerebellum when inertial terms are not considered in the non-preferred (A or C) direction
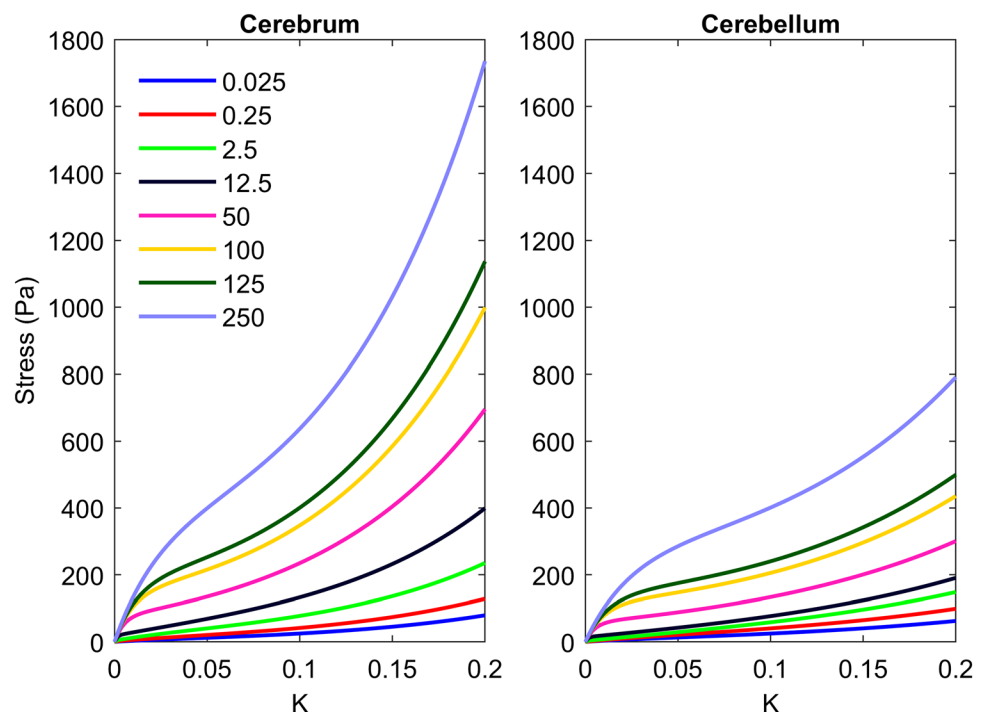
Although the preceding results show the ability of the presented model to fit the experimental data, its response to a loading scenario typical of TBI has not been shown. To examine its response to such loading, we simulated single ramp, simple shear using a single element model (homogeneous deformation; no inertial effects) for all the tested strain rates. Figure 12 shows the results for one of the non-preferred (*A* or *C*) directions. Notably, predicted cerebral stresses are markedly higher than cerebellar stresses at all rates and scale more at higher rates. The peak stress grows from 1.3 times higher in the cerebrum than the cerebellum at 0.025 s^{-1} to 2.2 times higher at a rate of 250 s^{-1}.

4 Discussion

The objective of this study was to develop anisotropic hyper-viscoelastic constitutive models of Göttingen minipig cerebrum and cerebellum tissue over a large range of strain rates relevant to conventional and blast TBI. Results show that the cerebrum and cerebellum are highly rate dependent and stiffen nonlinearly with strain rate. Additionally, results show that cerebrum and cerebellum are transversely isotropic. Samples showed high degrees of wave propagation during high rate oscillations, which complicated the constitutive model fitting with traditional optimization methods. However, dynamic inverse FE modeling was able to achieve adequate constitutive model fits.

4.1 Dynamic modulus and phase angle

Results show that brain tissue dynamic modulus increases exponentially as a function of strain rate. While we (Boiczyk et al. 2023), and multiple other studies (Darvish and Crandall 2001; Donnelly and Medige 1997; Nicolle et al. 2004; Nicolle et al. 2005; Rashid et al. 2013; Thibault and Margulies 1998), have previously demonstrated substantial rate dependence of brain tissue subject to simple shear (either single ramp or oscillatory loading), our previous modeling of Göttingen minipig brain tissue only captured loading at QS and high rates (150 and 300 s^{-1}); it was not characterized at intermediate rates relevant to portions of the brain that may not experience the most severe loads or to milder overall loading scenarios. Both Darvish and Crandall (Darvish and Crandall 2001) and Thibault and Margulies (Thibault and Margulies 1998) demonstrated a nonlinear increase in stiffness at frequencies between 1 and 1000 Hz and 20 and 200 Hz, respectively, with no drop off as seen in our data at a frequency of 80 Hz (100 s^{-1}), suggesting that signal noise may be affecting our results at these rates. Reported stress magnitudes at 100 Hz ranged from about 500–5000 Pa in previous studies compared to around 1000–4000 in our results, though direct comparisons are difficult due to differences in species, animal age, and time between death and sample testing.

Phase angle plots show a relatively stable phase shift between the stress and strain waveforms between rates of 0.025 and 12.5 s^{-1}, before the phase angle increases at 50 and 100 s^{-1}. Phase angle then decreases and becomes negative at the three highest rates as stress begins to lag strain. In a viscoelastic material subject to harmonic oscillation, stress should lead strain between 0 (purely elastic response) and 90 degrees (purely viscous response). At the two highest rates, our results show a negative phase angle, with strain leading stress, which was also demonstrated by Darvish and Crandall (2001) in porcine brain. This phenomenon suggests that inertial effects are present at high rates, which need to be accounted for. Namely, there is likely a substantial degree of wave propagation between the moving bottom plate and the fixed top plate where the load was measured, as the FE models predicted. However, because this was not immediately visible on test videos of high-rate tests, strains should be verified experimentally using digital image correlation (DIC) in future work. Preliminary evaluation of farm pig brain tissue and silicone gel with similar stiffnesses to brain tissue (Brands et al. 2002) cut to different heights suggests that the degree of this phase lag appears to be tied to sample height, with thicker samples showing a more pronounced degree of negative phase shift than thinner samples. This evaluation suggests that wave propagation, especially through the relatively thick samples tested here, was responsible for the unexpected behavior.

The increase in phase angle between 12.5 and 100 s^{-1} suggests that the internal damping (the tangent of the phase angle) increases as a function of driven frequency. This, in turn, violates the continuous relaxation spectrum assumption underlying the Fung quasi-linear viscoelastic (QLV) model (Fung 1993) used here, which states that internal damping will remain relatively constant between several decades of driven oscillatory frequencies. While the QLV models used in this work generally fit the data well, there was a noticeable trend toward overprediction of stresses at rates of 100 s^{-1} and above, especially in subsequent loading cycles, which may suggest models with increased damping at high rates may perform better. Although this effect is not as large in phase angle data calculated from the FE models, this may be a result of constitutive model selection rather than a physical property of the tissue. Future work should aim to explore constitutive models accounting for discontinuous damping, either through discrete element models (Budday et al. 2017b) or a fully nonlinear viscoelastic model (Darvish and Crandall 2001).

4.2 Anisotropy

Both the cerebrum and cerebellum were shown to be transversely isotropic, preferring the B direction, where DTI-identified fibers were oriented parallel to the shear plane but transverse to the direction of shear. Regional differences became more apparent as the strain rate increased, and the cerebrum appeared to have a larger degree of anisotropy than the cerebellum. Transverse isotropy was previously observed in this orientation in the brainstem by Arbogast and Margulies (Arbogast and Margulies 1998). Both Jin et al. (Jin et al. 2013) and Prange and Margulies (Prange and Margulies 2002) also tested samples from a portion of the corona radiata similar to our work. They found a significant difference in stiffness in a direction they suggest has a fiber orientation similar to the A direction in this work. However, both studies assumed that fibers predominantly ran outward (laterally and superiorly) from the corona radiata instead of rostral caudally, as the DTI we performed here shows, suggesting that the fiber orientation was closer to the B direction we found was stiffest. Conversely, both Budday et al. (2017a) and Nicolle et al. (Nicolle et al. 2005) showed no significant effect of direction in cerebral tissue. However, Budday tested tissue at QS rates where any variation between regions may be lost in natural variance. Nicolle tested tissue at either very low strains (0.0033%) or low rates (0.8 s^{-1}), conditions where directional differences may be difficult to detect.

4.3 Constitutive modeling

The FE models presented in this work show substantial shear wave propagation from the bottom surface, where oscillations were applied, to the top surface, the site of measurement. Examination of shear wave propagation through individual elements in the model of cerebellum suggests that it takes about 2.9 ms for the wave to travel the 5 mm from bottom to top at driven strain rates of 100, 125, and 250 s^{-1}, requiring a wave speed of 1.7 m/s. In comparison, a travel time of 2.4 ms, with a wave speed of 2.1 m/s, were calculated for the cerebrum model. The higher wave velocity in the cerebrum may explain the lower degree of phase shift seen in the MATLAB fit constitutive models between the cerebrum and cerebellum discussed in the Appendix. (Note that the phase shift discussed in connection with the MATLAB and inverse model fits is not the same as the phase angle presented with the dynamic modulus.) Jiang et al. (2015) measured acoustic shear wave speeds in porcine brain tissue exposed to ultrasonic radiation and reported shear wave speeds between 1.5 and 2 m/s; while, Hamhaber et al. (Hamhaber et al. 2007) reported a mean velocity of 1.88 ± 0.58 m/s in elastography experiments on human brain tissue subject to mechanical excitation of about 80 Hz (the driven frequency for the 100 s^{-1} tests reported here). These results agree with the results predicted by our FE simulations. As a result of the substantial wave propagation demonstrated here, future high-rate experiments on brain tissue should either aim to limit sample thickness to reduce the travel distance for shear waves or account for it during constitutive model fitting.

Unsurprisingly, the MATLAB constitutive model fits, which did not account for inhomogeneous deformations or dynamic effects, performed poorly. While the models performed well at rates below 125 s^{-1}, they underperformed the inverse FE fit models at all rates but 0.025, 100, and 125 s^{-1} in the cerebrum and 0.025 and 12.5 s^{-1} in the cerebellum. Critically, the poorly matched parameters at a high rate could lead to an inaccurate material response when used in dynamic simulations of brain injury, possibly making the tissue appear substantially stiffer. Additionally, the fourth invariant-dependent anisotropic model implemented in the inverse FE fit models could not be implemented using the modeling framework of the MATLAB models, as the assumption of a homogeneous, simple shear deformation would have led to no shear stress due to the fibers, with fiber stress only contributing axially. Anisotropy could be added by accounting for matrix–fiber interaction terms based on higher order invariants, but that may misrepresent the anisotropic response of the tissue given that inverse FE fit models could account for the observed direction dependence using just fiber terms.

While the inverse FE constitutive model fits performed better than the MATLAB fits, they still had substantial limitations. Inverse FE fits still show substantial error, especially at the lowest and highest rates, particularly regarding improper matching of model phase. While the phase shift is markedly improved from the MATLAB models at high rates, predicted stress waveforms still lead the experimental stress waveforms, suggesting an overprediction of wave velocity. The inverse FE fits also struggle to match amplitude through all oscillations at high rates. Future work should aim to improve these models by examining different constitutive models to address issues with damping and predicted wave amplitude.

The constitutive models presented here can predict the first two cycles of loading at all rates up to 125 s^{-1} and initial ramp loading at 250 s^{-1} in multiple fiber directions for both the cerebrum and cerebellum. At 250 s^{-1}, it is expected that the initial ramp loading could capture the initial blast overpressure wave seen in simulations of blast injury (Mao et al. 2015; Sundaramurthy et al. 2021), though could struggle predicting stresses from wave reflections.

4.4 Limitations

Experimentally recorded load data exhibited large degrees of variation at the QS (0.025 s^{-1}) and four highest (50–250 s^{-1})

rates. At the QS rate, the load data is subject to drift over the 300 s-long test, which seems to skew the results. While attempts were made to compensate for this drift during data post-processing, substantial preconditioning effects (i.e., stress softening) at this rate made it difficult to isolate the drift fully. As a result, data quality at this rate is diminished compared to subsequent rates but was still sufficient to be used to fit hyperelastic and anisotropic parameters, which showed little change in fit values when additional, higher-rate data were considered. The cerebrum shows a substantially larger degree of variation for all rates than the cerebellum, especially at 50 s^{-1}. Examination of individual stress traces shows a high degree of variation between the phase and amplitude of individual stress waveforms with no clear outliers at all rates. Given this group's harvesting location and testing orientation, animal-to-animal variations in overall fiber density and orientations, as well as slight variations in die location and rotation between brains, may be responsible for this.

At high rates, substantial noise becomes evident in load data, especially at the two highest rates where load data loses its roughly sinusoidal shape, and higher frequency oscillations can be seen in the data. While some degree of higher frequency oscillation is predicted by the FE models, suggesting that this could be an expected physical response of the tissue, it is also worth noting that frequency domain inspection of high-rate tests shows spikes close to the 410 Hz ringing frequency of the load cell-side test fixtures. Thus, it seems possible that some of the variations in high-rate tests may have been due to the influence of excitation of our load-cell-side test fixtures, resulting in poorer quality fitting. Future work at high rates should aim to use fixtures with higher ringing frequencies to reduce the risk of excitation.

In addition to issues with noise, the experimental data used in the creation of inverse FE models had a few notable limitations. Tissue deformations were not mapped during experiments and only the motion of the voice coil attached plate was simulated in the inverse FE models. Thus, the actual degree of wave propagation and inhomogeneous deformation predicted in the model cannot be experimentally validated. Moreover, this meant that we were unable to calculate the stress distribution throughout the material, potentially introducing error. Future work should aim to explicitly map sample deformations during tests using DIC to improve model quality. Inverse FE modeling coupled with DIC deformation data has previously been used to model brainstem, in compression (Felfelian et al. 2019), and soft tissue phantoms (Moerman et al. 2009) successfully, albeit at relatively low rates. Additionally, the experimental response used to fit constitutive models at all rates above the QS rate was substantially preconditioned and may not be representative of the in vivo state of the brain and may be substantially softened. Future work should aim to examine the effects of stress relaxation at high rates.

Appendix

Prior to work on inverse FE fitting, we attempted to fit constitutive models to the experimental data using numerical fitting methods in MATLAB. This was initially attempted using isotropic, hyper-viscoelastic models on samples tested in the non-preferred direction, assuming a homogeneous deformation. Due to limitations with this approach, we did not pursue definition of an anisotropic formulation.

Methods

As a first step, average data from the cerebrum and cerebellum in a non-preferred direction (direction A in Fig. 1) were used to fit a hyper-viscoelastic constitutive model (Puso and Weiss 1998) by optimizing an objective function in MATLAB, where the experimental deformation was assumed to be homogeneous. The 2nd Piola–Kirchhoff stress (S) was given by Eq. 6,

$$S(t) = \int_0^t G(t-s) \frac{\partial S^e}{\partial s} ds \tag{6}$$

where S^e is the elastic stress, and the reduced relaxation function $G(t)$ is given by a five-term Prony series (Eq. 7),

$$G(t) = 1 + \sum_{i=1}^5 g_i \exp\left(\frac{-t}{\tau_i}\right) \tag{7}$$

where g_1–g_5 are viscoelastic parameters, and τ_1–τ_5 are defined such that values vary by one decade from $\tau_1 = 1s$ to $\tau_5 = 10^{-4}s$. For the elastic stress, we used an incompressible one-term Ogden model, similar to our previous study (Boiczyk et al. 2023) (Eq. 8).

$$W = \frac{c}{m^2} \left(\lambda_1^m + \lambda_2^m + \lambda_3^m - 3\right) \tag{8}$$

The parameters c and m are the shear stiffness and a nonlinearity parameter, respectively; while, λ_i is the ith eigenvalue of the right Cauchy–Green stretch tensor. For this fitting, we assumed a homogeneous, simple shear deformation throughout the tissue (Eq. 9),

$$F = \begin{bmatrix} 1 & K & 0 \\ 0 & 1 & 0 \\ 0 & 0 & 1 \end{bmatrix} \tag{9}$$

where K is the shear strain calculated from the experimental displacement data (displacement divided by sample height).

The parameters c, m, and g_1–g_5 were fit in MATLAB using the function *fminsearchbnd* (D'Errico 2022) to optimize the objective function in Eq. 10. Prior to fitting, experimental 1st PK stress (P) was converted to 2nd PK stress.

$$\chi = \frac{1}{n_{\text{samp}}} \sum_{i=1}^{n_{\text{samp}}} \frac{\left(P_i^{\text{Experimental}} - P_i^{\text{Model}} \right)^2}{\max \left(P^{\text{Experimental}} \right)} \qquad (10)$$

Results

Constitutive models assuming a homogeneous deformation (simulated using MATLAB) performed well at rates of 0.025–12.5 s^{-1}, showing a low degree of phase shift and relatively low root mean squared error (RMSE) values for both the cerebellum (Fig. 13) and cerebrum (Fig. 14); phase angle and RMSE values for each model are shown in Table 4. At 50 s^{-1}, there is a noticeable increase in both

Fig. 13 Experimental data and MATLAB fits for the cerebrum in the *A* (non-preferred) direction

Fig. 14 Experimental data and MATLAB fits for the cerebellum in the *A* (non-preferred) direction

Table 4 Overall error (RMSE) and phase angle between regularized model and experimental stresses for the MATLAB model fits from the cerebrum and cerebellum in the non-preferred (A) direction

Region	Error mode	Strain rate (s^{-1})							
		0.025	0.25	2.5	12.5	50	100	125	250
Cerebrum	Phase (°)	1.4	−5.2	2.3	3.2	17.3	3.2	−12.4	−50.1
	RMSE	0.2	0.3	0.2	0.2	0.4	0.3	0.7	1.0
Cerebellum	Phase (°)	8.4	−2.0	2.0	7.5	16.4	−5.5	−13.8	−81.2
	RMSE	0.3	0.2	0.2	0.3	0.4	0.4	0.8	1.3

Negative phase shift denotes model leads experimental data

error and phase shift for both regions. At the two highest rates, there is a large, negative phase shift between the model and the experimental data, indicating that the model is predicting stress values occurring substantially earlier than observed experimentally, and suggesting that the assumption of a homogeneous deformation is incorrect. These models also poorly predict the general stress response at these highest rates, overpredicting the final two cycles at the 125 s^{-1} rate and substantially underpredicting stress values at the 250 s^{-1} rate.

Declarations

References

Arbogast KB, Margulies SS (1998) Material characterization of the brainstem from oscillatory shear tests. J Biomech 31:801–807. https://doi.org/10.1016/s0021-9290(98)00068-2

Bell ED, Converse M, Mao H, Unnikrishnan G, Reifman J, Monson KL (2018) Material properties of rat middle cerebral arteries at high strain rates. J Biomech Eng. https://doi.org/10.1115/1.4039625

Bilston L, Liu Z, Phan-Thien N (1997) Linear viscoelastic properties of bovine brain tissue in shear. Biorheology 34:377–385. https://doi.org/10.1016/s0006-355x(98)00022-5

Bilston L, Liu Z, Phan-Thien N (2001) Large strain behaviour of brain tissue in shear: Some experimental data and differential constitutive model. Biorheology 38:335–345

Boiczyk GM et al (2023) Rate- and region-dependent mechanical properties of gottingen minipig brain tissue in simple shear and unconfined compression. J Biomech Eng. https://doi.org/10.1115/1.4056480

Brands DW, Bovendeerd PH, Wismans JS (2002) On the potential importance of non-linear viscoelastic material modelling for numerical prediction of brain tissue response: test and application. Stapp Car Crash J 46:103–121. https://doi.org/10.4271/2002-22-0006

Brands DW, Bovendeerd PH, Peters GW (2000) Finite shear behavior of brain tissue under impact loading. Paper presented at the ASME International Mechanical Engineering Congress and Exposition, Orlando, Florida, USA,

Budday S et al (2017a) Mechanical characterization of human brain tissue. Acta Biomater 48:319–340. https://doi.org/10.1016/j.actbio.2016.10.036

Budday S, Sommer G, Haybaeck J, Steinmann P, Holzapfel GA, Kuhl E (2017b) Rheological characterization of human brain tissue. Acta Biomater 60:315–329. https://doi.org/10.1016/j.actbio.2017.06.024

Budde MD, Annese J (2013) Quantification of anisotropy and fiber orientation in human brain histological sections. Front Integr Neurosci 7:3. https://doi.org/10.3389/fnint.2013.00003

Centers for Disease Control and Prevention (2023) Traumatic brain injury & concussion. https://www.cdc.gov/traumaticbraininjury/get_the_facts.html. Accessed 10 Oct 2023

Chatelin S, Vappou J, Roth S, Raul JS, Willinger R (2012) Towards child versus adult brain mechanical properties. J Mech Behav Biomed Mater 6:166–173. https://doi.org/10.1016/j.jmbbm.2011.09.013

Darvish KK, Crandall JR (2001) Nonlinear viscoelastic effects in oscillatory shear deformation of brain tissue. Med Eng Phys 23:633–645. https://doi.org/10.1016/s1350-4533(01)00101-1

D'Errico J (2022) fminsearchbnd, fminsearchcon. Mathworks. https://www.mathworks.com/matlabcentral/fileexchange/8277-fminsearchbnd-fminsearchcon. Accessed September 15 2021 2021

Dixit P, Liu GR (2016) A review on recent development of finite element models for head injury simulations. Arch Comput Methods Eng 24:979–1031

Donnelly BR, Medige J (1997) Shear properties of human brain tissue. J Biomech Eng 119:423–432. https://doi.org/10.1115/1.2798289

Felfelian AM, Baradaran Najar A, Jafari Nedoushan R, Salehi H (2019) Determining constitutive behavior of the brain tissue using digital image correlation and finite element modeling. Biomech Model Mechanobiol 18:1927–1945. https://doi.org/10.1007/s10237-019-01186-6

Feng Y, Okamoto RJ, Namani R, Genin GM, Bayly PV (2013) Measurements of mechanical anisotropy in brain tissue and implications for transversely isotropic material models of white matter. J Mech Behav Biomed Mater 23:117–132. https://doi.org/10.1016/j.jmbbm.2013.04.007

Feng Y, Lee CH, Sun L, Ji S, Zhao X (2017) Characterizing white matter tissue in large strain via asymmetric indentation and inverse finite element modeling. J Mech Behav Biomed Mater 65:490–501. https://doi.org/10.1016/j.jmbbm.2016.09.020

Fung YC (1993) Biomechanics: mechanical properties of living tissues, 2nd edn. Springer, New York

Hamhaber U, Sack I, Papazoglou S, Rump J, Klatt D, Braun J (2007) Three-dimensional analysis of shear wave propagation observed by in vivo magnetic resonance elastography of the brain. Acta Biomater 3:127–137. https://doi.org/10.1016/j.actbio.2006.08.007

Hosseini-Farid M, Ramzanpour M, Ziejewski M, Karami G (2019) A compressible hyper-viscoelastic material constitutive model for human brain tissue and the identification of its parameters. Int J Non Linear Mech 116:147–154. https://doi.org/10.1016/j.ijnonlinmec.2019.06.008

Hosseini-Farid M, Ramzanpour M, McLean J, Ziejewski M, Karami G (2020) A poro-hyper-viscoelastic rate-dependent constitutive modeling for the analysis of brain tissues. J Mech Behav Biomed Mater. https://doi.org/10.1016/j.jmbbm.2019.103475

Hrapko M, van Dommelen JA, Peters GW, Wismans JS (2008) Characterisation of the mechanical behaviour of brain tissue in compression and shear. Biorheology 45:663–676. https://doi.org/10.3233/bir-2008-0512

Jiang Y, Li G, Qian LX, Liang S, Destrade M, Cao Y (2015) Measuring the linear and nonlinear elastic properties of brain tissue with shear waves and inverse analysis. Biomech Model Mechanobiol 14:1119–1128. https://doi.org/10.1007/s10237-015-0658-0

Jin X, Zhu F, Mao H, Shen M, Yang KH (2013) A comprehensive experimental study on material properties of human brain tissue. J Biomech 46:2795–2801. https://doi.org/10.1016/j.jbiomech.2013.09.001

Kaster T, Sack I, Samani A (2011) Measurement of the hyperelastic properties of ex vivo brain tissue slices. J Biomech 44:1158–1163. https://doi.org/10.1016/j.jbiomech.2011.01.019

Lujan TJ, Underwood CJ, Jacobs NT, Weiss JA (2009) Contribution of glycosaminoglycans to viscoelastic tensile behavior of human ligament. J Appl Physiol 106:423–431. https://doi.org/10.1152/japplphysiol.90748.2008

Maas SA, Weiss JA (2007) FEBio Theory Manual. https://help.febio.org/docs/FEBioTheory-4-0/. Accessed 16 Feb 2023

Maas SA, Ellis BJ, Ateshian GA, Weiss JA (2012) FEBio: finite elements for biomechanics. J Biomech Eng 134:011005. https://doi.org/10.1115/1.4005694

MacManus DB, Pierrat B, Murphy JG, Gilchrist MD (2017) Region and species dependent mechanical properties of adolescent and young adult brain tissue. Sci Rep. https://doi.org/10.1038/s41598-017-13727-z

Madhukar A, Ostoja-Starzewski M (2019) Finite element methods in human head impact simulations: a review. Ann Biomed Eng 47:1832–1854

Mao H, Unnikrishnan G, Rakesh V, Reifman J (2015) Untangling the effect of head acceleration on brain responses to blast waves. J Biomech Eng 137:124502. https://doi.org/10.1115/1.4031765

Meaney DF, Morrison B, Dale Bass C (2014) The mechanics of traumatic brain injury: a review of what we know and what we need to know for reducing its societal burden. J Biomech Eng. https://doi.org/10.1115/1.4026364

Military Health System DOD TBI Worldwide Numbers. https://health.mil/Military-Health-Topics/Centers-of-Excellence/Traumatic-Brain-Injury-Center-of-Excellence/DOD-TBI-Worldwide-Numbers. Accessed 10 Oct 2023

Moerman KM, Holt CA, Evans SL, Simms CK (2009) Digital image correlation and finite element modelling as a method to determine mechanical properties of human soft tissue in vivo. J Biomech 42:1150–1153. https://doi.org/10.1016/j.jbiomech.2009.02.016

Moran R, Smith JH, Garcia JJ (2014) Fitted hyperelastic parameters for human brain tissue from reported tension, compression, and shear tests. J Biomech 47:3762–3766. https://doi.org/10.1016/j.jbiomech.2014.09.030

Nicolle S, Lounis M, Willinger R (2004) Shear properties of brain tissue over a frequency range relevant for automotive impact situations: new experimental results. Stapp Car Crash J 48:239–258

Nicolle S, Lounis M, Willinger R, Palierne JF (2005) Shear linear behavior of brain tissue over a large frequency range. Biorheology 42:209–223

Prange MT, Margulies SS (2002) Regional, directional, and age-dependent properties of the brain undergoing large deformation. J Biomech Eng 124:244–252. https://doi.org/10.1115/1.1449907

Puso MA, Weiss JA (1998) Finite element implementation of anisotropic quasi-linear viscoelasticity using a discrete spectrum approximation. J Biomech Eng 120:62–70. https://doi.org/10.1115/1.2834308

Rashid B, Destrade M, Gilchrist MD (2013) Mechanical characterization of brain tissue in simple shear at dynamic strain rates. J Mech Behav Biomed Mater 28:71–85. https://doi.org/10.1016/j.jmbbm.2013.07.017

Simons M, Trajkovic K (2006) Neuron-glia communication in the control of oligodendrocyte function and myelin biogenesis. J Cell Sci 119:4381–4389. https://doi.org/10.1242/jcs.03242

Singh D, Cronin DS, Haladuick TN (2014) Head and brain response to blast using sagittal and transverse finite element models. Int J Numer Method Biomed Eng 30:470–489. https://doi.org/10.1002/cnm.2612

Subramaniam DR, Unnikrishnan G, Sundaramurthy A, Rubio JE, Kote VB, Reifman J (2021) Cerebral vasculature influences blast-induced biomechanical responses of human brain tissue front bioeng. Biotechnol 9:744808. https://doi.org/10.3389/fbioe.2021.744808

Sundaramurthy A, Alai A, Ganpule S, Holmberg A, Plougonven E, Chandra N (2012) Blast-induced biomechanical loading of the rat: an experimental and anatomically accurate computational blast injury model. J Neurotrauma 29:2352–2364. https://doi.org/10.1089/neu.2012.2413

Sundaramurthy A et al (2021) A 3-D finite-element minipig model to assess brain biomechanical responses to blast exposure. Front Bioeng Biotechnol. https://doi.org/10.3389/fbioe.2021.757755

Thibault KL, Margulies SS (1998) Age-dependent material properties of the porcine cerebrum: effect on pediatric inertial head injury criteria. J Biomech 31:1119–1126. https://doi.org/10.1016/s0021-9290(98)00122-5

Velardi F, Fraternali F, Angelillo M (2006) Anisotropic constitutive equations and experimental tensile behavior of brain tissue. Biomech Model Mechanobiol 5:53–61. https://doi.org/10.1007/s10237-005-0007-9

Weickenmeier J, de Rooij R, Budday S, Ovaert TC, Kuhl E (2017) The mechanical importance of myelination in the central nervous system. J Mech Behav Biomed Mater 76:119–124. https://doi.org/10.1016/j.jmbbm.2017.04.017

Wu T, Hajiaghamemar M, Giudice JS, Alshareef A, Margulies SS, Panzer MB (2021) Evaluation of tissue-level brain injury metrics using species-specific simulations. J Neurotrauma 38:1879–1888. https://doi.org/10.1089/neu.2020.7445

Yeh FC, Verstynen TD, Wang Y, Fernandez-Miranda JC, Tseng WY (2013) Deterministic diffusion fiber tracking improved by quantitative anisotropy. PLoS ONE 8:e80713. https://doi.org/10.1371/journal.pone.0080713

Zhang L, Makwana R, Sharma S (2013) Brain response to primary blast wave using validated finite element models of human head and advanced combat helmet. Front Neurol 4:88. https://doi.org/10.3389/fneur.2013.00088

Zhao W, Choate B, Ji S (2018) Material properties of the brain in injury-relevant conditions—experiments and computational modeling. J Mech Behav Biomed Mater 80:222–234. https://doi.org/10.1016/j.jmbbm.2018.02.005